Performance of turbulence closures for vortex interaction physics over military aircraft

Michel Visonneau*, Emmanuel Guilmineau*, and Ginevra Rubino*
*ECN/CNRS, LHEEA, Nantes/France
michel.visonneau@ec-nantes.fr

1 Introduction

Modern air tactics require agile maneuverability capability that includes operations at high angles of attack and sideslip. Military air vehicles routinely develop multiple, close-proximity vortices within required operating conditions. Interactions among these vortices, between the vortices and the vehicle components, and at high speeds, between the vortices and shock waves significantly affect maneuver performance, often with adverse consequences. Current capability to predict these effects with CFD is inadequate, and some aspects of the vortex-interaction flow physics are not well understood. The NATO/AVT-316 collaborative research ahs been built to assess the capability of current CFD methods to predict vortex-interaction effects, extend our understanding of vortex-interaction flow physics for these problems through numerical and physical experimentation. In the framework of this general collaborative effort, this article gives a glimpse of the current studies undertaken by the authors after one year of collaboration.

2 ISIS-CFD at a glance

The solver ISIS-CFD, available as a part of the FINE^{TM}/Marine computing suite distributed by NUMECA Int., is an incompressible unsteady Reynolds-averaged Navier-Stokes (URANS) method mainly devoted to marine hydrodynamics. The method features several sophisticated turbulence models: apart from the classical two-equation k-ϵ and k-ω models, the anisotropic two-equation Explicit Algebraic Reynolds Stress Model (EARSM), as well as Reynolds Stress Transport Models (RSTM), are available, see Deng and Visonneau (1999) and Duvigneau and Visonneau (2003), with or without rotation corrections. All models are available with wall-function or low-Reynolds near wall formulations. Hybrid RANS-LES turbulence models based on Detached Eddy Simulation (DES-SST, IDDES) are also implemented, see Guilmineau et al. (2013), and have been validated on automotive flows characterized by large separations. The solver is based on a finite volume method to build the spatial discretization of the transport equations. The second order accurate unstructured discretization is face-based. While all unknown state variables are cell-centered, the systems of equations used in the implicit time stepping procedure are constructed face by face. Pressure-velocity coupling is enforced through a Rhie & Chow SIMPLE type method. Free-surface flow is simulated with a multi-phase flow approach: the water surface is captured with a conservation equation for the volume fraction of water, discretized with specific compressive discretization schemes, see Queutey and Visonneau (2007). The technique included for the six degrees of freedom simulation of ship motion is described by Leroyer and Visonneau (2005). Many possibilities of grid management are included like morphing, sliding and overlapping grids. Finally, an anisotropic automatic grid refinement procedure has been developed which is controlled by various flow-related criteria, see Wackers et al. (2014). Parallelization is based on domain decomposition using the MPI (Message Passing Interface) protocol.

3 Description of the test case and numerical setup

Airtbus Defence and Space and the Technical University of Munich are in charge of the measurements on a model military aircraft studied in the framework of the Research Technical Group NATO/AVT-316 (Hitzel et al. (2019), Pfnür et al. (2019)). The model is shown in Figure 1. Experiments are conducted in a wind tunnel for a speed of 51.97 m/s, which leads to a Mach number of 0.15, a value for which it is still reasonable to use an incompressible flow solver. Drag, lift, sideslip forces and moments are measured at several angles of attack ranging from 4° to 40° . Up to now, 0° and 5° sideslip angles are considered. PIV measurements are also conducted at 16° and 24° angles of attack without sideslip. Sixteen cross-sections covering the wing have been chosen where the three velocity components, the longitudinal vorticity and

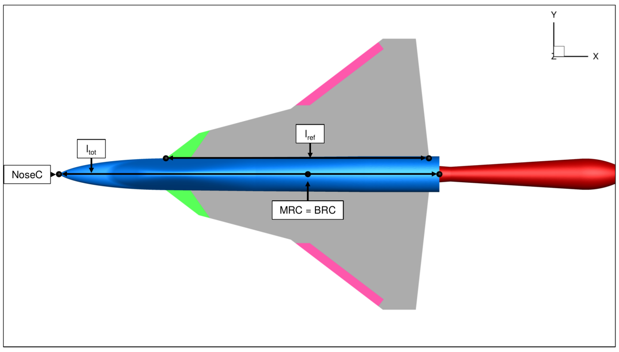

Fig. 1: Main characteristics of the model

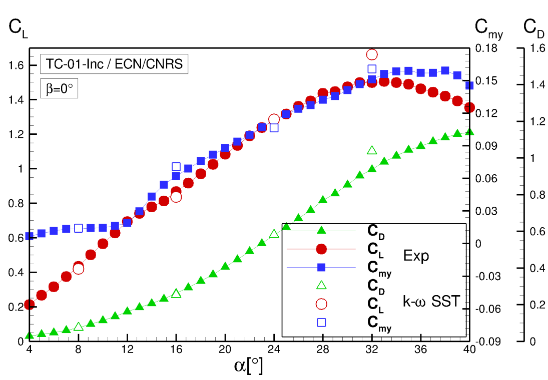

Fig. 2: $k-\omega$ SST - Drag, lift and pitching moment at various angles of attack

the turbulence kinetic energy are measured. Specific refined zones across the core of the vortices have been defined to follow the onset and progression of the various vortices present in the flow configurations of interest.
The computations performed with ISIS-CFD make an intensive use of the automatic mesh refinement procedure based on the Hessian of the flux in order to build a mesh with a controlled high density in the core of the vortices. For instance, some cross-sectional views of the adapted grids are shown in Figure 6 for various turbulence closures.

4 Global analysis at various angles of attack

Figure 2 shows a comparison between the computations of drag, lift and pitch moment and measurements. In these first computations, only the $k-\omega$ SST closure is used. The agreement is very good for almost all incidences but one can notice a degradation of the agreement for higher incidences.
Figure 3 shows the different topologies of the flow over the wing for four angles of incidence (8° , 16° , 24° and 32°). This figure provides a global view of the three-dimensional vortical structures which are created, progress and and interact along the wing. The vortices are represented as isosurfaces of the dimensionless second invariant $Q^* = 50$ and the red surface inside the vortices correspond to the region where a flow reversal is observed. All these computations are performed with $k-\omega$ SST turbulence model. At 8° , no interaction takes place between the two vortices emanating from the wing leading edge and no flow reversal is observed in the core of these vortices. At 16° , the interaction between the two main vortices is observed in the second half of the wing and is accompanied by a flow reversal in the core of the largest vortex. At 24° , a third vortex generated at the fore part of the aircraft, progresses along the fuselage and is suddenly diverted to interact with the two vortical structures already present at lower angles of attack. Flow reversal is observed earlier in the same vortex as previously. At 32° , a fourth vortex progresses close to the one which appeared at 24° . Both vortices are violently diverted away from the fuselage and interact with the aforementioned third vortex. At this angle of attack, flow reversal in the largest vortex appears very close to the leading edge. It is worthwhile to mention that once the flow reversal takes place, no coherent vortical structure can be observed. Moreover, these computations based on a linear isotropic turbulence closure ($k-\omega$ SST without any rotation correction) do not necessarily reflect the true physics of these flows, especially at high angles of attack as indicated, at least, by the degraded agreement with measured forces and moment.

5 Angle of attack 16°

In order to understand the reasons of the deteriorated agreement between measured and computed forces and pitching moment at high angle of attack, it is necessary to proceed to a local analysis of the flow and try to relate global data to local flow characteristics. Since the automatic grid refinement is used, one can consider that the discretisation error is kept unrelatively low in the vortices and their neighborhood. However, nothing is known on the modelling error associated with the turbulence closure. This is the

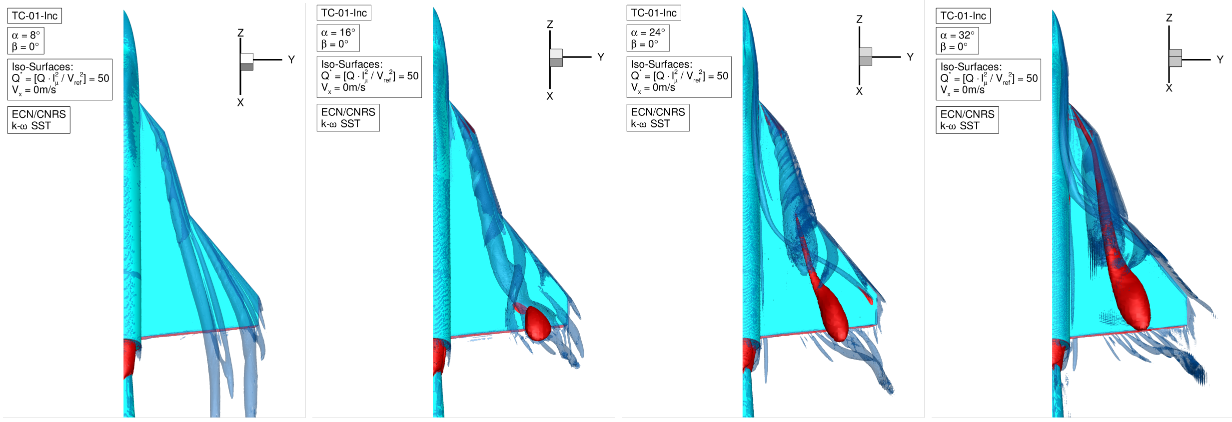

(a) 8° (b) 16° (c) 24° (d) 32°

Fig. 3: $k - \omega$ SST - Main vortical structures at various angles of attack

reason why it has been decided to perform a systematic study of turbulence closures at a selected angle of attack of 16° for which PIV experiments were available. Our objective is to assess/compare the performances of various turbulence closures and make some recommendations. In this study, three models are studied, ranging from the linear isotropic $k - \omega$ SST model Menter (1994), an explicit anisotropic Reynolds stress closures built by the authors in the late 90's Deng and Visonneau (1999) and a recent Reynolds Stress Transport model Cecora et al. (2015). First of all, Table 1 shows a comparison between measured and computed forces and moments for these three turbulence models encompassing most of the available RANS modeling strategies. In this table, S stands for simulation, D for experimental data and $E = S - D[\%D]$ provides the percentage of error with the measured data. One can notice that the best prediction of forces and moment is provided by the RSTM model while the EARSM model developed by ECN/CNRS behaves very well for the forces but is less accurate on the prediction of the pitching moment. The number of cells reached once the adaptive grid process has converged is 36.5M for $k - \omega$ SST, 51.5M for EARSM and 124.6M for SSGLRR RSTM turbulence models over a half-aircraft. Figure 4 shows the three-dimensional vortices represented by Q^*=50 and the location of the flow reversal in the core of vortices for an angle of attack of 16° while Figure 5 shows the wall pressure distribution and the skin-friction lines. The interaction between vortices takes place almost at the same location, independently of the turbulence closures. However, the vortices predicted by SSGLRR are more intense and less diffused. We can observe the influence of the vortex interaction on the shape of the skin friction lines on $k-\omega$ SST and RSTM results but not on the EARSM prediction. RSTM results exhibit a more pronounced convergence, associated with a more intense open separation. Figure 4 shows that flow reversal occurs near the trailing edge with $k - \omega$ SST while no reverse flow is visible with the anisotropic turbulence models. Figure 6 shows the meshes in a cross-section $x/Cr = 0.592$ obtained once the adaptive mesh refinement procedure has converged. The locations and regions of high shear of both vortices of interest are clearly visible on the meshes, which illustrate the remarkable efficiency of such a methodology. For the SSGLRR RSTM model, the adaptive mesh refinement leads to a very dense concentration of points

Table 1: AoA 16° - Forces and moment

α=16°	C_D		C_L		C_{my}	
β=0°	S	E	S	E	S	E
Experiments (D)	0.2620		0.8580		0.0622	
k-ω SST	0.2553	-2.55%	0.8372	-3.59%	0.0707	13.71%
EARSM	0.2627	0.25%	0.8674	-0.11%	0.0524	-15.66%
SSGLRR-ω	0.2639	0.70%	0.8612	-0.82%	0.0651	4.78%

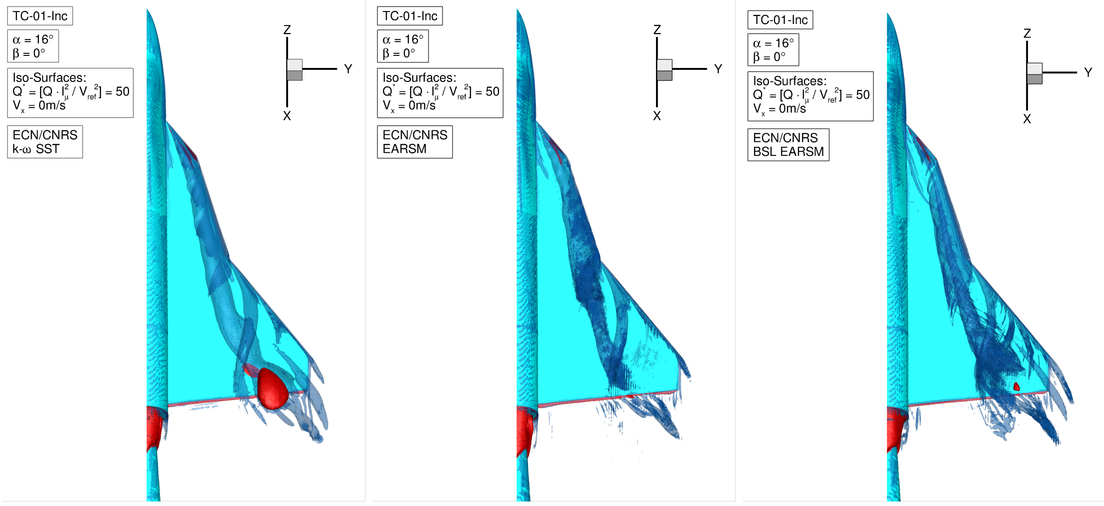

(a) k-ω SST (b) EARSM (c) SSGLRR-ω

Fig. 4: AoA 16° - Influence of the turbulence closure on the main vortical structures characteristics

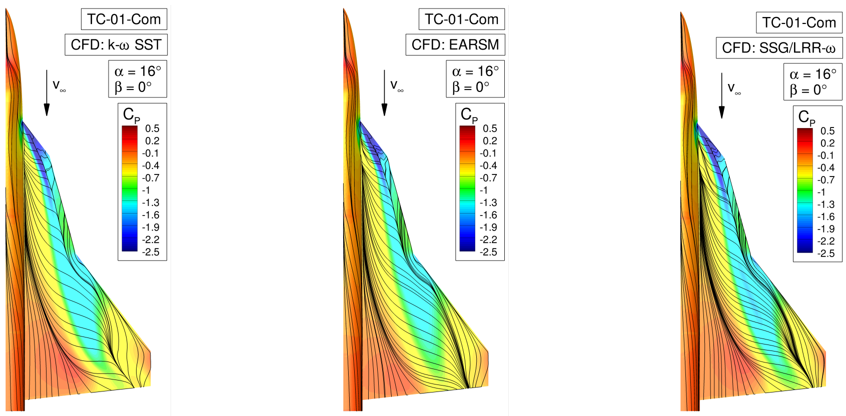

(a) k-ω SST (b) EARSM (c) SSGLRR-ω

Fig. 5: AoA 16° - Influence of the turbulence closure on the wall pressure distribution and friction lines

in the core of the vortices for unclear reasons at the time of writing this paper. Figure 7 to Figure 9 show at the same location, the cross-sectional distributions of U, ω_x, and tke obtained with the same turbulence closures to be compared with TUM PIV measurements. The best overall distribution of U contours is obtained with the SSGLRR RSTM model although the low value of the velocity (blue region) in the core of the first vortex is not captured. EARSM appears to behave better from that standpoint but the size of the region where U is low appears to be overestimated in comparison with measurements. Moreover, the higher velocity region above the previous region, is not captured by EARSM while it is correctly simulated by SSGLRR and to a lesser extent by k-ω SST. Figure 8 shows the cross-sectional distribution of ω_x. It is clear that the magnitude of the longitudinal vorticity is under-estimated by the linear isotropic $k-\omega$ SST model, which is not surprising. On the other hand, SSGLRR RSTM provides a higher longitudinal vorticity in good agreement with the experiments for the second vortex but slightly over-estimated for the first vortex. EARSM seems to behave relatively well as long as one can judge from this global picture. Finally, Figure 9 shows the cross-sectional distribution of the turbulence kinetic energy, tke. This is a very important data to assess the physical consistency of a turbulence model in the core of vortices since it is difficult to get a correct agreement both on the longitudinal vorticity and tke. Very often, the rotation corrections aiming at increasing the longitudinal vorticity cause a local decay of tke in the core of the vortex which is not necessarily in agreement with the measurements (see Visonneau et al. (2018)

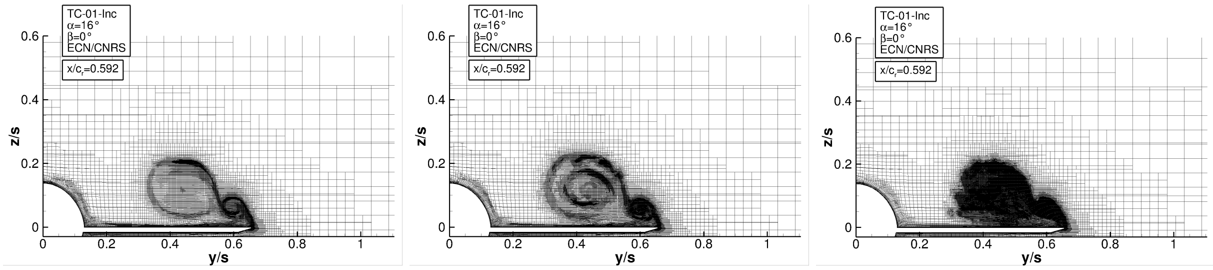

(a) k-ω SST (b) EARSM (c) SSGLRR-ω

Fig. 6: AoA 16° - Local mesh density at $x/c_\mathrm{r} = 0.592$

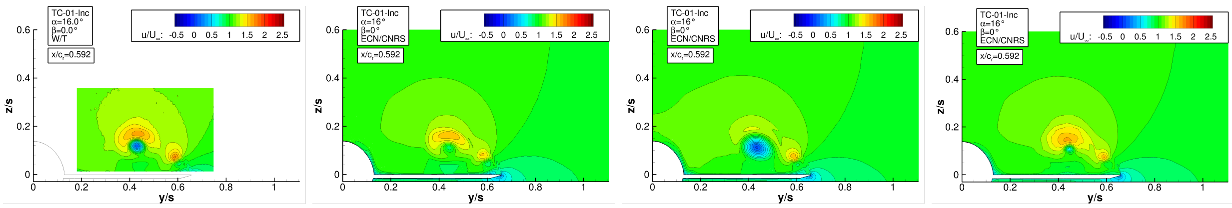

(a) Experiments (b) k-ω SST (c) EARSM (d) SSGLRR-ω

Fig. 7: AoA 16° - Axial velocity at $x/c_\mathrm{r} = 0.592$

for an extensive computational study of the local core flow physics of a vortex emanating from the sonar dome of a US Navy frigate at static drift). Although the preliminary TUM measurements of tke should be considered with care, one can observe that the core with a significant tke region is smaller in the experiments than in the simulations. $k - \omega$ SST predicted tke distribution is very homegeneous with a minimum in the core of the vortex, which is not in agreement with TUM measurements. Both EARSM and RSTM predict a higher value of tke in the core of both vortices, with a significantly higher local value for SSGLRR RSTM. Globally, this distribution complies better with the measurements, although the local value of tke appears to be significantly over-estimated. At this stage, it is difficult to go further in the analysis since TUM has to check if the measured tke distribution takes into account enough small flow scales to be considered accurate enough for a detailed turbulence closure assessment. However, it should be mentioned that, contrary to what is observed for U and ω_x in the core of a vortex, tke is a quantity for which very large differences can be observed between different categories of turbulence closures.

6 Conclusion

The flow over a military aircraft at high incidence is very complex and characterized by vortex interaction even if at 16° , the interaction is relatively weak. The preliminary results presented here illustrate a very first attempt to compare several turbulence models on meshes for which the discretization error should not play a prominent role. It leads us to realize how difficult it is to simulate accurately the vortex core flow physics. The onset and progression of vortices appear to be strongly dependent on the turbulence model. Although the most sophisticated turbulence model based on Reynolds Stress Transport Equations appear to provide the most intense vortices, no turbulence model is able to provide a satisfactory agreement on all the experimental data of interest in the core of vortices. A more complete analysis of the flows and additional computations based on hybrid RANS/LES will be presented during the symposium.

Acknowledgements

The computations were performed using HPC resources from GENCI (Grand Equipement National de Calcul Intensif) (Grant-A0042A00129, Grant-A0062A00129), which is gratefully acknowledged. The experimental data were provided in the framework of the NATO-STO task group AVT-316 by Airbus

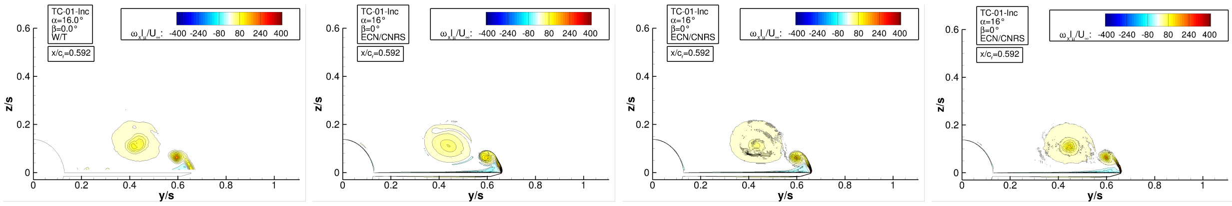

(a) Experiments (b) k-ω SST (c) EARSM (d) SSGLRR-ω

Fig. 8: AoA 16° - Axial vorticity at $x/c_\mathrm{r} = 0.592$

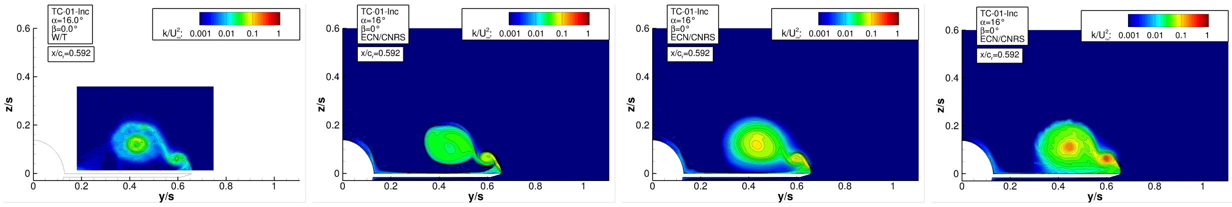

(a) Experiments (b) k-ω SST (c) EARSM (d) SSGLRR-ω

Fig. 9: AoA 16° - Turbulence kinetic energy at $x/c_\mathrm{r} = 0.592$

Defence and Space (Aerodynamic Design, TEAGA-TL6) and the University of Munich (Chair of Aerodynamics, (TUM-AER)).

References

G. Deng and M. Visonneau (1999). Comparison of Explicit Algebraic Stress Models and Second-Order Turbulence Closures for Steady Flows around Ships. *Proc. 7th Int. Conf. on Numerical Ship Hydrodynamics*, Nantes, France.

R. Duvigneau and M. Visonneau (2003). On the Role Played by Turbulence Closures in Hull Shape Optimization at Model and Full Scale. *J. Mar. Sci. Technol.*, **8**, 11–25.

E. Guilmineau, O. Chikhaoui, G. Deng and M. Visonneau (2013). Cross Wind Effects on a Simplified Car Model by a DES Approach. *Computers & Fluids*, **78**, 2013, 29–40.

A. Leroyer, and M. Visonneau (2005). Numerical Methods for RANSE Simulations of a Self-Propelled Fish-like Body. *J. Fluid & Structures*, **30-3**, 975–991.

P. Queutey, and M. Visonneau (2007). An Interface Capturing Method for Free-Surface Hydrodynamic Flows. *Computers & Fluids*, **36**, 1481–1510.

J. Wackers, G. Deng, E. Guilmineau, A. Leroyer, P. Queutey, and M. Visonneau (2014). Combined Refinement Criteria for Anisotropic Grid Refinement in Free-Surface Flow Simulation. *Computers & Fluids*, **92**, 209–222.

F. Menter (1994). Two-equation eddy-viscosity turbulence models for engineering applications. *AIAA Journal*, **32-8**, 1598–1605.

R.-D. Cecora, R. Radespiel, B. Eisfeld, B. and A. Probst (2015). Differential Reynolds-Stress Modeling for Aeronautics. *AIAA Journal*, **53-3**, 739–755.

S. Pfnür, C. Breitsamter (2019). Leading-Edge Vortex Interactions at a Generic Multiple Swept-Wing Aircraft Configuration. *Journal of Aircraft (Review number: C035491)*, accepted for publication.

S.M. Hitzel, A. Winkler, A. Hövelmann (2019). Vortex Flow Aerodynamic Challenges in the Design Space for Future Fighter Aircraft. To appear in *New Results in Numerical and Experimental Fluid Mechanics XII*, published by Springer.

M. Visonneau, E. Guilmineau and G. Rubino (2018). Computational Analysis of the Flow around a Surface Combatant at 10° Static Drift and Dynamic Sway Conditions. *Proc. 32nd Symposium on Naval Hydrodynamics*, Hamburg, Germany.